

How the toughness in metallic glasses depends on topological and chemical heterogeneity

Qi An^a, Konrad Samwer^{b,c}, Marios D. Demetriou^b, Michael C. Floyd^b, Danielle O. Duggins^b, William L. Johnson^{b,1}, and William A. Goddard III^{a,1}

^aMaterials and Process Simulation Center, California Institute of Technology, Pasadena, CA 91125; ^bKeck Engineering Laboratories, California Institute of Technology, Pasadena, CA 91125; and ^cFirst Institute of Physics, University of Goettingen, 37077 Goettingen, Germany

Contributed by William A. Goddard III, May 13, 2016 (sent for review March 8, 2016; reviewed by Takeshi Egami and Evan Ma)

To gain insight into the large toughness variability observed between metallic glasses (MGs), we examine the origin of fracture toughness through bending experiments and molecular dynamics (MD) simulations for two binary MGs: Pd₈₂Si₁₈ and Cu₄₆Zr₅₄. The bending experiments show that Pd₈₂Si₁₈ is considerably tougher than Cu₄₆Zr₅₄, and the higher toughness of Pd₈₂Si₁₈ is attributed to an ability to deform plastically in the absence of crack nucleation through cavitation. The MD simulations study the initial stages of cavitation in both materials and extract the critical factors controlling cavitation. We find that for the tougher Pd₈₂Si₁₈, cavitation is governed by chemical inhomogeneity in addition to topological structures. In contrast, no such chemical correlations are observed in the more brittle Cu₄₆Zr₅₄, where topological low coordination number polyhedra are still observed around the critical cavity. As such, chemical inhomogeneity leads to more difficult cavitation initiation in Pd₈₂Si₁₈ than in Cu₄₆Zr₅₄, leading to a higher toughness. The absence of chemical separation during cavitation initiation in Cu₄₆Zr₅₄ decreases the energy barrier for a cavitation event, leading to lower toughness.

cavitation | bulk metallic glass | molecular dynamics simulations | toughness

Engineering ceramics are strong, with high yield strength, but suffer from brittleness. In contrast, crystalline metals tend to have high fracture toughness because dislocation motion promotes plastic deformations that suppress cracks propagations, but concomitantly this dislocation motion reduces yield strength. Metallic glasses (MGs) tend to have high strength, and for some compositions, the high strength is accompanied by a high fracture toughness, making MGs promising engineering materials (1). The fracture toughness in MGs, which is accommodated by shear banding and limited by cavitation, is thought to arise from initiation of a crack opening at the core of an extending shear band (2–4). Then, new high-strength and high-toughness MGs may be designed by identifying compositions capable of suppressing cavitation during shear band extension. However, the complex physics of cavitation in MGs has obscured the development of models to illustrate cavitation's origin.

For MGs, cavitation leads to the crack opening process that controls directly the fracture toughness, a fundamental property for material design and applications. Since the first amorphous alloy (Au₇₅Si₂₅) reported at the California Institute of Technology in 1960 (5), tremendous effort has been dedicated to understand why the amorphous structure leads to such excellent mechanical properties as high elastic limit, yield strength, and hardness (2, 6). However, toughness, which varies dramatically between MG compositions, ranging from values typical of brittle ceramics to those typical of engineering metals (2, 6, 7), is still poorly understood. More recently, improved alloys have been developed that demonstrate very high toughness, including a bulk Pd-rich, Si-bearing glass, Pd₇₉Ag_{3.5}P₆Si_{9.5}Ge₂ (7), and a bulk Zr-rich, Cu/Al-bearing glass, Zr₆₁Ti₂Cu₂₅Al₁₂ (8), in which shear band plasticity suppresses crack opening.

The fracture resistance of MGs is understood to arise from a competition between two processes: shear band plasticity and void

nucleation. Currently, the process of shear band plasticity is widely recognized to be accommodated by the cooperative shearing of local atomic clusters [shear transformation zones (STZs)] (9, 10). However, to describe the fracture process, a condition for cavitation is needed coupled with the description of shear band plasticity to account for a crack opening along an operating shear band. Recently, Rycroft and Bouchbinder (11) coupled a continuum STZ model with a condition for cavitation to describe the fracture of MGs. The authors found that cavitation plays an essential role in the initiation of fracture, where they found a crack to evolve by successive void nucleation events along an operating shear band. In the context of molecular dynamics (MD) simulations, we and others proposed that cavitation precedes the onset of crack formation at the core of an operating shear band (12–15).

Our previous study showed that cavitation in metallic liquids is a homogeneous process that can be described with our revised classical nucleation theory (CNT) that incorporates the Tolman length correction (12). Furthermore, Falk et al. showed that our revised CNT remains valid down to picosecond time scales, whereas strain-aging effects become important at longer time scales in MGs (13). Murali et al. found that fracture in a brittle MG is governed by nanoscale void nucleation and coalescence (14), whereas Wang et al. established a correlation between shear transformations and dilatation (15). However, despite the success in numerical calculations, the atomistic origins of the cavitation process in MGs remains obscure, especially the role of topological structure and chemistry. Recent progress has been made to understand the nature of the atomic structures in MGs (16–18). Furthermore, Ding et al. examined the correlation between local atomic packing structure and quasilocated soft modes correlated with STZ (19). The authors found that the geometrically unfavored motifs (GUMs) contribute

Significance

This article reports and explains how the cavitation in metallic glasses is controlled by topological structure as well as chemical heterogeneity. It is shown that in the tough metal-metalloid Pd-Si metallic glass, cavitation initiation is controlled by both chemical separation and particular types of low coordination number (LCN) Pd-centered polyhedra. In contrast, cavitation in the brittle metal-metal Cu-Zr metallic glass is only governed by topological factors. A high-energy barrier to form LCN polyhedra and the process of chemical separation during cavitation initiation are believed to contribute to a higher metallic glass toughness, thereby allowing a larger plastic strain to fracture.

Author contributions: Q.A., W.L.J., and W.A.G. designed research; Q.A., K.S., M.D.D., M.C.F., D.O.D., and W.A.G. performed research; Q.A. and W.L.J. analyzed data; and Q.A., K.S., M.D.D., M.C.F., D.O.D., W.L.J., and W.A.G. wrote the paper.

Reviewers: T.E., University of Tennessee; and E.M., Johns Hopkins University.

The authors declare no conflict of interest.

¹To whom correspondence may be addressed. Email: wlj@caltech.edu or wag@wag.caltech.edu.

This article contains supporting information online at www.pnas.org/lookup/suppl/doi:10.1073/pnas.1607506113/-DCSupplemental.

the most to the soft modes that might lead to shear transformations (19). These GUMs prefer to concentrate in the quasilocalized soft spots that promote widespread shear transformations under external stress (20). Thus, although MGs lack long-range order, there is evidence that both short-range order (SRO) and medium-range order (MRO) play essential roles in determining such properties of MGs as glass-forming ability (GFA), elasticity, and strength/hardness (16–20). To understand the role of SRO and MRO on the fracture process of MGs, it is essential to establish the relationship between local cluster morphology and cavitation processes.

The present work combines mechanical testing experiments with MD simulations to investigate the origin of the large variability in toughness observed between MG compositions (2, 6, 7). For ease of simulation and analysis, we chose to study binary MGs. Two MG compositions were chosen that are capable of forming bulk rods (1–2 mm in diameter) such that the MGs can be mechanically tested. The two binary MGs chosen are $\text{Cu}_{46}\text{Zr}_{54}$, a metal-metal alloy in which metallic bonding dominates, and $\text{Pd}_{82}\text{Si}_{18}$, a metal-metalloid alloy in which chemical SRO is well established (21). We synthesized 1-mm-diameter rods of $\text{Cu}_{46}\text{Zr}_{54}$ and $\text{Pd}_{82}\text{Si}_{18}$ and performed bending experiments to assess the rods' bending ductility. Then, we used MD simulations to study the cavitation mechanisms and cluster packing (chemical and topological SRO) effects in these two types of MGs at various conditions of tension and shear under negative pressure. Lastly, the difference in ductility between the two MGs is rationalized in terms of the differences in their cavitation mechanisms and cluster-packing effects.

Results and Discussion

Processing and Testing of $\text{Pd}_{82}\text{Si}_{18}$ and $\text{Cu}_{46}\text{Zr}_{54}$. To quantitatively measure the fracture toughness of MGs in accordance with established standards, samples considerably thicker than 1–2 mm are generally needed. Therefore, it would not be possible to quantitatively assess the fracture toughness of the chosen MGs in any meaningful way, because glass formation is limited to 1- to 2-mm-diameter rods. Nonetheless, one can semiquantitatively estimate a critical mode I stress intensity factor, K_{IC} , from knowledge of the plastic strain to failure in bending (i.e., the bending ductility). Conner et al. (22) derived an analytical expression to evaluate K_{IC} in bending of unnotched MGs by relating K_{IC} to the bending strain at fracture. The underlying assumption in the authors' analysis is that a stable crack developing at the core of an operating shear band is akin to a precrack, and hence when such crack develops, the bending test transitions to a fracture toughness test of a [single-edge notched bending SEN(B)] specimen.

To avoid any adverse effects on toughness from extrinsic parameters such as crystallinity, oxygen, and impurities, the alloy ingots were prepared using high-purity elements with low-oxygen content and were alloyed under an ultrapure inert atmosphere (*Supporting Information*). The MG test samples were carefully inspected by X-ray diffraction and differential scanning calorimetry to ensure the absence of crystallinity. Samples for the two MGs were synthesized differently because of their different melt reactivity with crucible materials. Specifically, MG rods of $\text{Cu}_{46}\text{Zr}_{54}$ were produced by arc-melting over a water-cooled copper hearth followed by suction casting in a copper mold, whereas MG rods of $\text{Pd}_{82}\text{Si}_{18}$ were produced by furnace melting in quartz capillaries, followed by rapid water quenching. Because the latter method produces a somewhat lower cooling rate (because of a slower heat removal rate across the low conductivity quartz walls), the $\text{Pd}_{82}\text{Si}_{18}$ MG rods are associated with a lower quenched-rate state in relation to $\text{Cu}_{46}\text{Zr}_{54}$. Because fracture toughness is known to depend on the processing cooling rate (23), the fracture toughness of the $\text{Pd}_{82}\text{Si}_{18}$ MG rods may be expected to be somewhat depressed relatively to $\text{Cu}_{46}\text{Zr}_{54}$ because of a lower quenched-rate state.

Three rods of each MG were tested in three-point bending (*Supporting Information*). A representative bending load-

displacement diagram of each MG is presented in Fig. 1A. Because the loading and specimen geometries were identical for the two samples, the values for load and displacement are direct reflections of stress and strain. Within the elastic region, the load-displacement slopes are roughly equal, indicating approximately the same Young's moduli, which is consistent with the measured Young's moduli of the two alloys (24). On the other hand, the load at yielding is higher for $\text{Cu}_{46}\text{Zr}_{54}$ than $\text{Pd}_{82}\text{Si}_{18}$ by about 15%, indicating a higher yield strength. Within the plastic regime, the $\text{Cu}_{46}\text{Zr}_{54}$ sample fractures soon after it yields, demonstrating a rather limited ductility. In contrast, the $\text{Pd}_{82}\text{Si}_{18}$ sample continuously deforms plastically to a very large displacement without fracturing, indicating a very high plastic strain in the absence of fracture and hence a very high ductility. This picture was consistent in all three samples tested for each alloy. Specifically, the bending displacement to fracture for all three $\text{Cu}_{46}\text{Zr}_{54}$ samples was found to be between 0.4 and 0.6 mm, whereas all $\text{Pd}_{82}\text{Si}_{18}$ samples exceeded 1.2 mm in bending displacement (which is the maximum displacement applicable by the bending fixture) without fracturing. Through the concept of Conner et al. (22), one can therefore conclude that $\text{Pd}_{82}\text{Si}_{18}$ has a considerably higher fracture toughness compared with $\text{Cu}_{46}\text{Zr}_{54}$, because the plastic strain attainable before fracture is considerably larger. Moreover, considering that the $\text{Pd}_{82}\text{Si}_{18}$ samples are associated with a somewhat lower quench rate state in relation to $\text{Cu}_{46}\text{Zr}_{54}$, the difference in the intrinsic fracture toughness may be even larger than the difference in bending ductility suggests.

To identify the dominant micromechanisms at play in these bending experiments, we examined the tension side of the rods using scanning electron microscopy (SEM). The micrograph of a fractured $\text{Cu}_{46}\text{Zr}_{54}$ rod (Fig. 1B) shows a catastrophic crack adjacent to a few shear bands, revealing that only a very limited number of shear bands were generated before crack opening. Careful inspection of the fracture surfaces did not reveal presence of any preexisting pores or inclusions that may have triggered premature fracture (Fig. S1). Therefore, one can conclude that the ductility and toughness of $\text{Cu}_{46}\text{Zr}_{54}$ is intrinsically low.

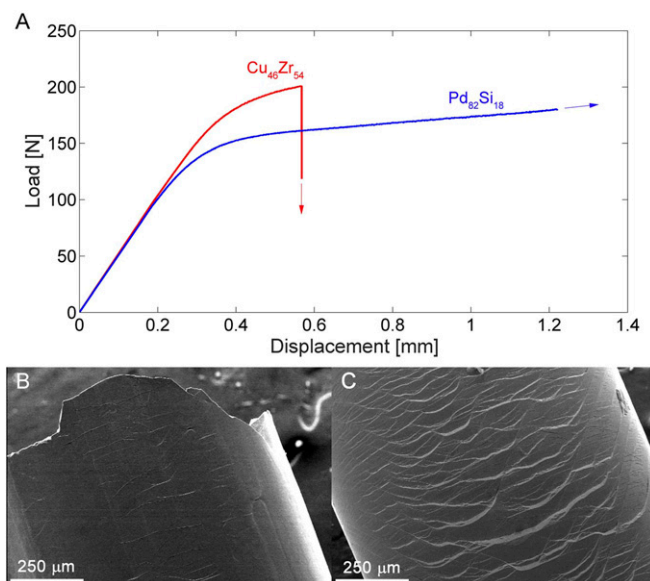


Fig. 1. (A) Bending load-displacement diagram for 1-mm-diameter amorphous rods of $\text{Pd}_{82}\text{Si}_{18}$ and $\text{Cu}_{46}\text{Zr}_{54}$. (B) SEM image on the tension side of the fractured $\text{Cu}_{46}\text{Zr}_{54}$ rod showing the catastrophic crack adjacent to a few shear bands. (C) SEM image on the tension side of the deformed $\text{Pd}_{82}\text{Si}_{18}$ rod showing a dense network of shear bands and absence of any opening or microcrack.

In contrast, the micrograph of the deformed Pd₈₂Si₁₈ rod (Fig. 1C) reveals a dense network of shear bands and absence of any opening or microcrack, which is consistent with the high ductility and toughness revealed in the bending experiment.

MD Simulations on the Cavitation of Pd₈₂Si₁₈ and Cu₄₆Zr₅₄ Under Hydrostatic Tension. To investigate the origin of the different toughness of these two types of MGs, we performed the MD simulations of the initial stage of the cavitation. We started with amorphous structures for Cu₄₆Zr₅₄ and Pd₈₂Si₁₈ using periodic super cells, containing 32,000 atoms. We used two approaches to induce cavitation:

- i) Application of hydrostatic tension at a constant strain rate of $2.0 \times 10^8 \text{ s}^{-1}$
- ii) Shear at a constant strain rate of $1.0 \times 10^{10} \text{ s}^{-1}$ applied under negative overall pressure

Twenty independent simulations for tension and seven independent simulations for shear were performed to obtain good statistics.

The stress–strain relationships extracted from the MD simulations (Fig. 2A) indicate that the stress/strain slope, which is a measure of the bulk modulus, is $\sim 52\%$ larger for Pd₈₂Si₁₈ compared with Cu₄₆Zr₅₄. This difference is roughly consistent with the measured bulk moduli of the two alloys (24). Under hydrostatic tension, we find that the negative pressure (tension) increases to a maximum of -12.9 GPa for Pd₈₂Si₁₈ and to -11.0 GPa for Cu₄₆Zr₅₄, at which point, cavitation events initiate to relax the negative pressure very quickly. The higher cavitation pressure for Pd₈₂Si₁₈ indicates that it requires more mechanical work to introduce an opening process for crack formation than does Cu₄₆Zr₅₄, leading to a higher fracture toughness in Pd₈₂Si₁₈. This difference explains the observed higher fracture toughness of Pd₈₂Si₁₈ from experiments.

Cavitation in MGs is controlled by the spatial heterogeneity in the glass, initiating at preferential nucleation sites (10). To locate the preferred cavitation sites, we started with the largest nanovoid within the bulk MGs just after initiating cavitation and traced this backward in time. This nanovoid evolution is shown in Fig. 2B for Pd₈₂Si₁₈. Based on the evolution of the largest nanovoid, the cavitation event involves the following steps.

- i) Firstly, the location within the MGs of largest void site changes with time until the cavity location is selected at time **ts**, after which, the largest void is always at the same site.
- ii) Secondly, the size of this largest void fluctuates with time between **ts** and time **tc**.
- iii) Finally, at **tc**, cavitation initiates with the cavity growing monotonically with time.

Thus, the time **tc** is the critical time for cavitation. Time **ts** should be important only in very local regions at the MD scale because there must be many cavitation sites at the macroscopic scale. This cavitation process is similar in Cu₄₆Zr₅₄, as discussed below.

The chemical bonding is quite different in Pd₈₂Si₁₈ and Cu₄₆Zr₅₄. In Pd₈₂Si₁₈, the Si atoms tend to form strong covalent bonds with neighbor Pd atoms, whereas the Pd atoms tend to form weak metallic bonds among themselves. Thus, we expect that cavitation would initiate from Pd-rich regions making initiation of cavitation strongly dependent on chemical heterogeneity. This expectation is confirmed by our analysis of the nearest neighbor composition surrounding the largest nanovoid, as shown in Fig. 2C. In particular, the fraction of Pd neighbors at the largest nanovoid is nearly 100% before **ts** and then decreases quickly within a few picoseconds to 92% at **ts**. Then, as the largest void is growing after **ts**, the ratio of the Si component increases monotonically but remains much lower than the average ratio, until failure occurs (**tc**). These chemical fluctuations in the Pd can be explained from the Pd-Si

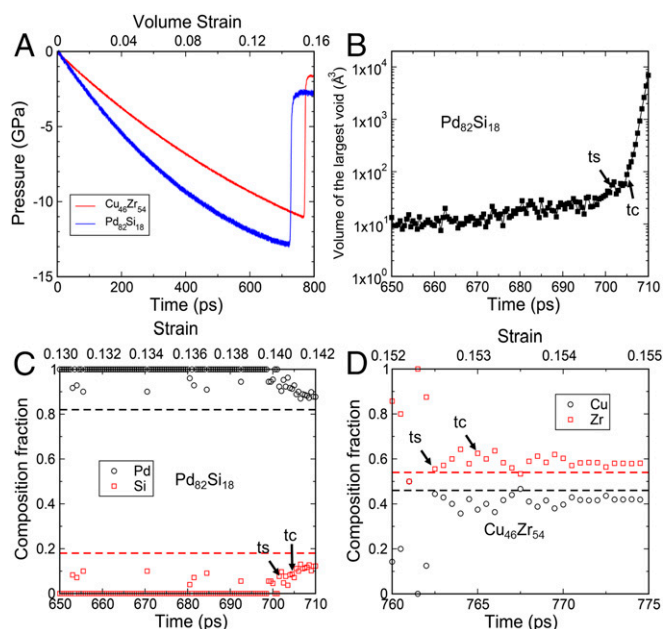


Fig. 2. Tension-driven cavitation events for Pd₈₂Si₁₈ and Cu₄₆Zr₅₄. (A) Typical case showing the pressure as a function of time (strain) for a uniformly increasing hydrostatic tension. (B) The size of the largest void for Pd₈₂Si₁₈ as a function of time for the case in A. From **ts** to later times, the largest void remains at the same site, but cavitation starts at time **tc**. The time interval between **ts** and **tc** varies within 30 ps for 20 cases as shown in Table S1. (C) The chemical character near the largest void for Pd₈₂Si₁₈. (D) The chemical character near the largest void for Cu₄₆Zr₅₄.

phase diagram [American Society for Metals (ASM) Alloy Phase Diagram Database; mio.asminternational.org/apd/index.aspx], which shows that the Pd₈₂Si₁₈ amorphous phase lies between the pure Pd face-centered cubic crystal and the ordered Pd₃Si crystal. Thus, we find that the Pd composition in the largest void fluctuates between 100% and 82%.

In contrast, in the Cu-Zr phase diagram (ASM Alloy Phase Diagram Database; mio.asminternational.org/apd/index.aspx), the Cu₄₆Zr₅₄ amorphous phase lies between the Cu₁₀Zr₇ crystal and the CuZr₂ crystal (33%–59% for Cu), leading to no obvious chemical trends. This speculation is confirmed by our chemical analysis of the largest nanovoid for Cu₄₆Zr₅₄, as shown in Fig. 2D, where the Cu ratios near the largest nanovoid fluctuate between 33% and 46%.

To determine the level of chemical heterogeneity responsible for initiating cavitation, we analyzed a minimum rectangular region ($8.8 \times 9.7 \times 7.0 \text{ \AA}^3$) containing all nearest-neighbor atoms of the cavity configuration at time **tc**, finding that the Pd concentration is 88.6%. As the critical nanovoid expands, this local enhanced Pd concentration decreases toward the bulk ratio, as shown in Fig. 3A. This decrease indicates that the chemical heterogeneity sufficient to initiate cavitation is localized within a very narrow region of $\sim 2.0 \text{ nm}^3$. A similar analysis on the structure at ambient conditions (without tension) shows an even more localized chemical heterogeneity within $\sim 1.0 \text{ nm}^3$. Thus, we propose that a criterion for predicting the location of the cavitation site is that the Pd concentration be greater than 87% in the structure at ambient conditions. To validate this criterion, we located cavitation sites for the 20 independent tension simulations and mapped them back to the original intact structure. As shown in Fig. 3B, all cavitation sites are within a Pd-rich region that satisfy this $>87\%$ criterion for the Pd concentration.

To validate these ideas about the effects of local chemical heterogeneity on cavitation in Pd₈₂Si₁₈, we created a different

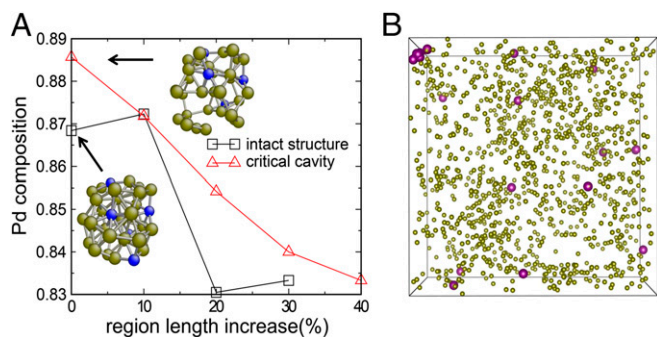


Fig. 3. Chemical analysis and the related cavitation sites for $\text{Pd}_{82}\text{Si}_{18}$. The Pd and Si atoms are represented by yellow and blue balls, respectively. (A) The Pd composition distribution as the increase of the near cavity region. (B) The cavitation sites (purple balls) in the intact system.

initial configuration with the same composition by randomly exchanging 5% of the Pd with Si atoms, followed by 2.0 ns of equilibrium using the isothermal–isobaric (NPT) ensemble. The different structure is well in equilibrium after 2.0 ns as shown in Fig. S2. The Pd concentration distributions of two configurations in Fig. S3 A and B show a flatter distribution for the other configuration with more Pd-rich sites, indicating less SRO. The cavitation times for these two structures lead to a normal distribution (Fig. S3 C and D) in which the $t_c = 658.4$ ps for the structure with more Pd-rich sites, compared with the previous value of $t_c = 719.1$ ps. This difference indicates that the increased number of Pd-rich sites significantly reduces the cavitation time (strain) by $\sim 8.4\%$. The results show that the cavitation behavior of the same $\text{Pd}_{82}\text{Si}_{18}$ composition can differ substantially even with the same composition, depending instead on local fluctuations in chemical composition.

To characterize the topological SRO, we use a Voronoi tessellation analysis (25). The types and fractions of Si-centered and Pd-centered polyhedra for the intact $\text{Pd}_{82}\text{Si}_{18}$ and evolution under tension before failure are given in Figs. S4 and S5, with the details discussed in the *Supporting Information*. Here, we focus on the polyhedral clusters containing large free volumes. For $\text{Pd}_{82}\text{Si}_{18}$, we considered only the low coordination number Pd-centered polyhedra (termed as “LCN-Pd-polyhedra”), with less than 10 nearest neighbors and with only one or no Si atoms. A typical structural evolution during cavitation of these polyhedral clusters is shown in Fig. 4A,

where the number of LCN-Pd-polyhedra around the cavity increases from three at time t_s (701.5 ps) to seven at time t_c (704.5 ps), which then breaks up at 705 ps. Note that the cavities are surrounded by a 4–11 LCN-Pd-polyhedra for all 20 independent cavitation events, as listed in Table S1. Generally, the number of LCN-Pd-polyhedra around the cavity increases from t_s to t_c for the sites at which cavitation later occurs. The average size of the LCN-Pd-polyhedra is \sim seven polyhedra, and the average critical volume is 68 \AA^3 . The main types of LCN-Pd-polyhedra are (0 3 6 0), (0 4 4 0), and (0 4 4 1), which belong to the Bernal holes class (26), constituting 78% of the total LCN-Pd-polyhedra. The critical volume increases as the number of LCN-Pd-polyhedra increases, as shown in Fig. 4B.

To characterize the cavity shape, we measured the distance between cavity center and the polyhedral center, as shown in Fig. 4C. The largest distance is 5.54 \AA , whereas the smallest distance is only 2.64 \AA , indicating that the cavity shape is spheroidal. We found that cavitation preferentially breaks bonds along one direction rather than isotropic 3D dilation. As the cavity grows to a larger size, it becomes more spherical because of the surface tension.

Shear Induced Cavitation in $\text{Pd}_{82}\text{Si}_{18}$. To mimic shear induced cavitation in $\text{Pd}_{82}\text{Si}_{18}$, we applied shear deformation on the pretension system with a tensile strain of 0.12. Here, we pretension the system to observe cavitation within the MD timescale. Fig. 5A shows the pressure and the shear stress in the shear-driven cavitation event. We observe that the pressure decreases from -11.3 to -9.9 GPa within the first 20 ps, indicating a structural relaxation process. The shear stress also increases to -1.0 GPa within the first 10 ps. The negative pressure decreases suddenly at 225 ps, indicating a cavitation event. The shear process accelerates the initiation of cavitation. We confirmed this acceleration by another MD simulation in which we kept a fixed pressure of -9.9 GPa. Here, no cavitation was observed within 2 ns.

For the shear-driven cavitation event, the size and positions of the largest void displays a similar character to that for tension, where the local cavitation is selected at time t_s and cavitation initiates at time t_c , as shown in Fig. 5B. The chemistry is also similar showing a preferred cavitation site within the Pd-rich region, as shown in Fig. 5C. The structural evolution of LCN-Pd-polyhedra surrounding the cavity center is shown in Fig. 5D. As the cavity size increases continuously from 214.5 to 221 ps, the number of LCN-Pd-polyhedra around cavity increases from two to seven. We examined seven independent shear-driven cavitation events with the results listed in Table S2 and shown in Fig. 4 B and C.

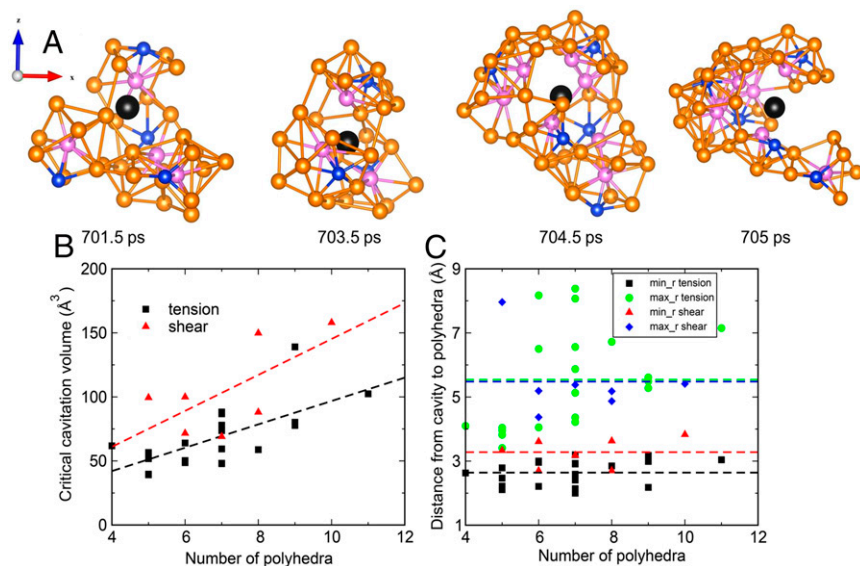


Fig. 4. The LCN-Pd-polyhedra cluster surrounding the critical cavities. (A) The evolution of LCN-Pd-polyhedra cluster surrounding the cavity center. (B) The relation between the number of LCN-Pd-polyhedra and the critical cavitation volume at t_c . (C) Shape-related information about the critical cavity at t_c , indicating that the critical cavity is spheroidal shape. The cavity center, Pd atoms, Si atoms, and Pd-center atoms are represented by black, yellow, blue, and pink balls, respectively.

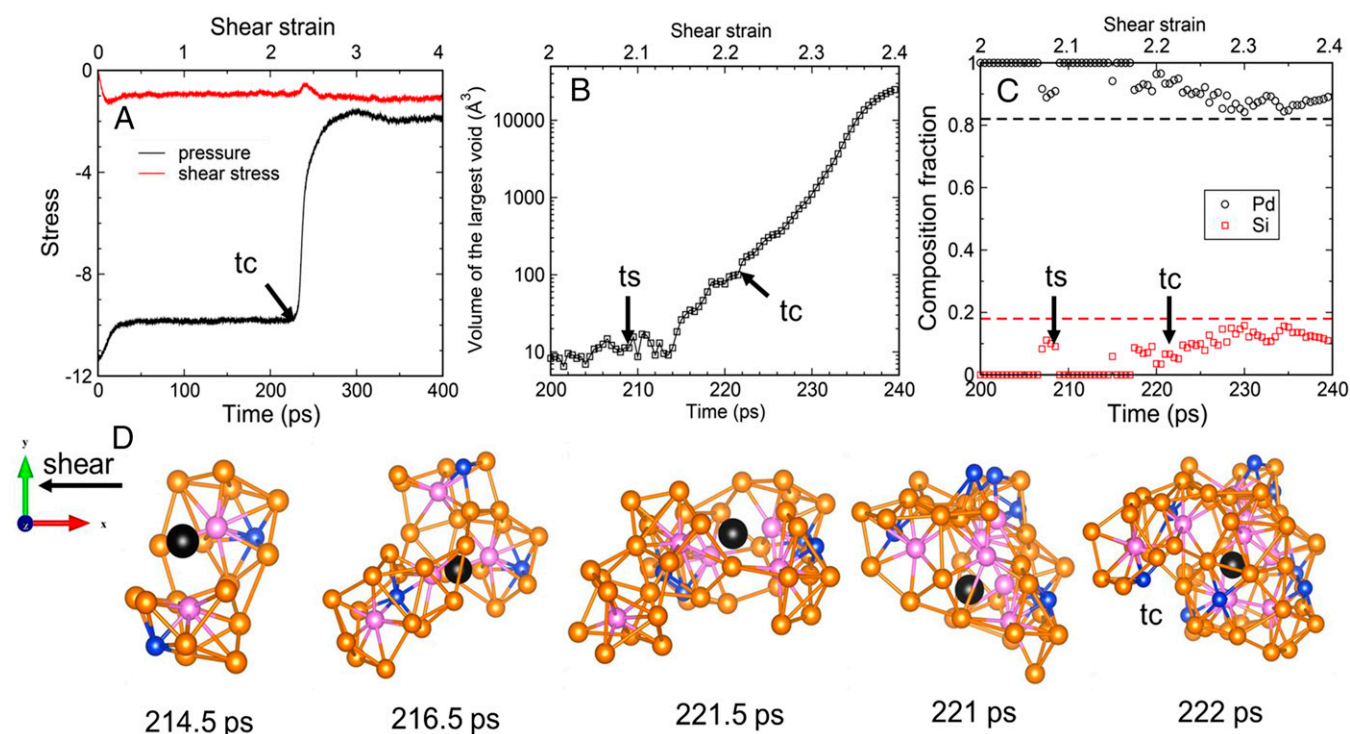


Fig. 5. Shear-induced cavitation for $\text{Pd}_{82}\text{Si}_{18}$. (A) Pressure and shear stress evolution. (B) The size evolution of the largest void. (C) The chemistry near the largest void. (D) The structures of LCN-Pd-polyhedra clusters surrounding the cavity center. The cavity center is black, the Pd atoms are yellow, the Si atoms are blue, and the Pd-center atoms are pink.

Our shear-driven cavitation simulations show character comparable with our tension simulations. However, the critical cavitation volume for shear is 56% larger than for tension, with the volume of LCN-Pd-polyhedra increasing from 68 to 106 \AA^3 , as shown in Fig. 4B. This increase is because the minimum distance between cavity center and the polyhedral cluster center increases by 14% or 3.2 \AA under shear but only 2.8 \AA in tension and the maximum distances of 5.4 and 5.5 \AA are almost the same for shear and tension, as shown in Fig. 4C.

Cavitation-Rate Estimations From Transition State Theory and MD Simulations. Our simulations show that the cavitation process can be described in terms of droplet formation with the cavitation rates estimated using our modified CNT (10, 12). However, the accumulation of LCN-Pd-polyhedra near the critical cavity leads to broken bonds preferentially along a particular

direction leading to an anisotropic cavity shape, making it hard to estimate the surface energy for use in the formula for the cavitation rates (12). Alternatively, we can consider the cavitation events as rate-dependent events that can be treated by activation theory.

We used the critical cavity in Fig. 4A as an example. Through the calculations of the potential energy, virial pressure, and Voronoi volume of these LCN-Pd-polyhedra, we obtain an activation enthalpy of 0.31 eV per atom. Here, we ignore the entropy effects and estimate the prefactor value as $5.0 \times 10^{11} \text{ ps}^{-1}$. Then we obtain a cavitation rate of $6.0 \times 10^{42} \text{ s}^{-1} \cdot \text{m}^{-3}$. From the MD simulations, the average cavitation time is estimated to be $\sim 10 \text{ ps}$ and the possible cavitation sites (centers of Pd-rich polyhedral clusters where Pd content is above 87%) are estimated to be 6,000. Thus, the direct measurement of the cavitation rate from MD simulations is $3.3 \times 10^{43} \text{ s}^{-1} \cdot \text{m}^{-3}$, which is consistent with the estimation from

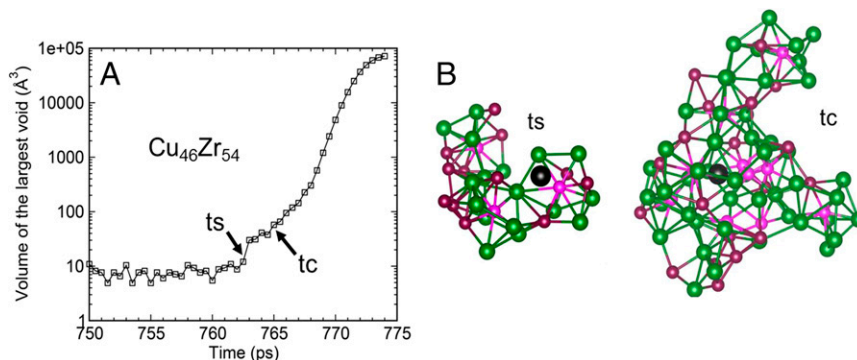


Fig. 6. Tension-driven cavitation events for $\text{Cu}_{46}\text{Zr}_{54}$. (A) The size evolution of the largest void. (B) The structures of LCN-Cu-polyhedra cluster surrounding the cavity center. The cavity center, Cu, Zr, and Cu-center atoms are represented by black, purple, green, and pink balls, respectively.

transition state theory. The details of this calculation are in the [Supporting Information](#).

Topological Analysis of Cavitation in $\text{Cu}_{46}\text{Zr}_{54}$. Because chemical factors are less obvious for $\text{Cu}_{46}\text{Zr}_{54}$, we focus on the topological analysis of cavitation. As shown in Fig. 6, the number of LCN-polyhedra increases from three at time **ts** to nine at time **tc**, similar to $\text{Pd}_{82}\text{Si}_{18}$. However, the polyhedral type are all Cu-centered polyhedral clusters with the main types being (0 3 6 0), (0 4 4 0), and (0 4 4 1), constituting 56% of the total for this particular case. These low coordination Cu-centered polyhedra (LCN-Cu-polyhedra) have been developed from the competing motifs (27) in the intact structures under hydrostatic tension, with the fluctuation of the composition in the range of 33–46 at% Cu. This lack of chemical factors playing a role in $\text{Cu}_{46}\text{Zr}_{54}$ should decrease the energy requirement for a cavitation event from that of $\text{Pd}_{82}\text{Si}_{18}$, leading to an earlier onset of crack formation and a lower fracture toughness in $\text{Cu}_{46}\text{Zr}_{54}$ than $\text{Pd}_{82}\text{Si}_{18}$, as observed experimentally.

Cavitation Nucleation in $\text{Pd}_{82}\text{Si}_{18}$ and $\text{Cu}_{46}\text{Zr}_{54}$. In $\text{Cu}_{46}\text{Zr}_{54}$, the LCN-Cu-polyhedra with coordination numbers (CNs) of 8 and 9 develop faster because of the absence of chemical heterogeneity. As the polyhedra aggregate in a local region above a critical concentration, cavitation initiates from these weak sites.

In contrast to $\text{Cu}_{46}\text{Zr}_{54}$, the cavitation nucleation in $\text{Pd}_{82}\text{Si}_{18}$ is delayed by two factors. First, deformation-induced LCN-Pd-polyhedra in $\text{Pd}_{82}\text{Si}_{18}$ is more difficult than that of LCN-Cu-polyhedra in $\text{Cu}_{46}\text{Zr}_{54}$. In this Pd-rich composition, local packing is dominated by Si-centered tricapped trigonal prism and Pd-centered polyhedra with CNs of 12 or 13. For Si-centered polyhedra, the covalent character of Si makes them rather rigid and highly resistant to deformation. For Pd, it is hard to decrease the CN around Pd to form LCN polyhedra because the local environment change makes only subtle difference in CN within this Pd-rich region. So the rate of forming low CN polyhedra is lower than the case for $\text{Cu}_{46}\text{Zr}_{54}$. Secondly, chemical partitioning is required to form the high Pd concentration region. This phase separation is facilitated by stress-assisted “diffusion” via nonaffine displacements in shear transformations. This diffusion-like “relocation of atoms to observable segregation” process has to be accrued via many shear transformations in prolonged deformation. This process further delays the cavitation initiation, which is triggered by the weak spots.

A previous study showed that the $\text{Fe}_{80}\text{P}_{20}$ MG is very brittle compared with the relatively more ductile $\text{Cu}_{50}\text{Zr}_{50}$ MG (14). The

brittle behavior in the $\text{Fe}_{80}\text{P}_{20}$ glass is associated with forming multiple nanoscale cavities, which arise from atomic scale spatial fluctuations of the local density (14). In the more ductile $\text{Cu}_{50}\text{Zr}_{50}$ glass, extensive shear banding tends to suppress crack propagation. In the current study, we showed that the $\text{Pd}_{82}\text{Si}_{18}$ glass is even more ductile than $\text{Cu}_{46}\text{Zr}_{54}$ glass, owing to local chemical heterogeneities and providing an additional barrier for cavitation. The common conclusion from both studies is that the intrinsic cavitation mechanism effectively controls fracture toughness.

In summary, our bending experiments revealed that $\text{Pd}_{82}\text{Si}_{18}$ is far more ductile and tougher than $\text{Cu}_{46}\text{Zr}_{54}$. The higher toughness of $\text{Pd}_{82}\text{Si}_{18}$ arises from an ability to deform plastically in the absence of crack nucleation through cavitation. Our MD simulations revealed that in $\text{Cu}_{46}\text{Zr}_{54}$, cavitation is mainly governed by the types of similar Cu-centered polyhedron. However, in $\text{Pd}_{82}\text{Si}_{18}$, cavitation is controlled by both this topological structure of particular types of Pd-centered polyhedron plus local chemical heterogeneity. Together, these two factors lead to the higher observed toughness. Thus, we find that cavitation initiation in $\text{Pd}_{82}\text{Si}_{18}$ requires formation of very Pd-rich regions. However, the bonding to Si tends to distribute the Pd inhomogeneously, thereby forming far fewer Pd-rich clusters than expected statistically. Consequently, to initiate cavitation in $\text{Pd}_{82}\text{Si}_{18}$, it is necessary for Pd to diffuse to form these Pd-rich clusters. The slow kinetics of the Pd-diffusion process raises the overall energy barrier for a cavitation event, which enables more extensive plastic strains before fracture, leading to a higher fracture toughness for $\text{Pd}_{82}\text{Si}_{18}$. This conclusion suggests that if one attempts to optimize the roles of chemical inhomogeneity and topology in the process of cavitation and crack opening, new tougher MG compositions may be developed. Chemical factors might also play essential roles in the nucleation process of crystallization in MGs, thus controlling their GFA.

Supporting Information. The [Supporting Information](#) includes (i) details regarding processing and testing, (ii) simulation details and analysis methods, (iii) the Voronoi tessellation analysis for $\text{Pd}_{82}\text{Si}_{18}$, (iv) details regarding cavitation-rate estimations from transition state theory and MD simulations, (v) fractography of $\text{Cu}_{46}\text{Zr}_{54}$ specimens, (vi) [Figs. S1–S5](#), and (vii) [Tables S1 and S2](#).

ACKNOWLEDGMENTS. This work was supported by Defense Advanced Research Projects Agency Grant W31P4Q-13-1-0010 (to program manager, John Paschkewitz), the Army Research Laboratory under Cooperative Agreement W911NF-12-2-0022 [Materials in Extreme Dynamic Environments (MEDE)], and National Science Foundation Grant Division of Materials Research (DMR)-1436985 (to program manager John Schlueter).

- Greer AL (2011) Metallic glasses: Damage tolerance at a price. *Nat Mater* 10(2):88–89.
- Lewandowski JJ, Wang WH, Greer AL (2005) Intrinsic plasticity or brittleness of metallic glasses. *Philos Mag Lett* 85(2):77–87.
- Xi XK, et al. (2005) Fracture of brittle metallic glasses: Brittleness or plasticity. *Phys Rev Lett* 94(12):125510.
- Cui JW, Calin M, Eckert J, Zhang ZF (2013) Tensile fracture dynamics and intrinsic plasticity of metallic glasses. *Appl Phys Lett* 102:031908.
- Klement W, Willens RH, Duwez P (1960) Non-crystalline structure in solidified gold-silicon alloys. *Nature* 187:869–870.
- Ashby MF, Greer AL (2006) Metallic glasses as structural materials. *Scr Mater* 54(3):321–326.
- Demetriou MD, et al. (2011) A damage-tolerant glass. *Nat Mater* 10(2):123–128.
- He Q, et al. (2012) Crack-resistance curve of a Zr-Ti-Cu-Al bulk metallic glass with extraordinary fracture toughness. *Acta Mater* 60(12):4940–4949.
- Argon AS (1979) Plastic deformation in metallic glasses. *Acta Metall* 27(1):47–58.
- Falk ML, Langer JS (1998) Dynamics of viscoplastic deformation in amorphous solids. *Phys Rev E Stat Phys Plasmas Fluids Relat Interdiscip Topics* 57:7192–7205.
- Rycroft CH, Bouchbinder E (2012) Fracture toughness of metallic glasses: Annealing-induced embrittlement. *Phys Rev Lett* 109(19):194301.
- An Q, et al. (2011) Atomistic characterization of stochastic cavitation of a binary metallic liquid under negative pressure. *J Phys Chem Lett* 2(11):1320–1323.
- Guan P, Lu S, Spector MJB, Valavala PK, Falk ML (2013) Cavitation in amorphous solids. *Phys Rev Lett* 110(18):185502.
- Murali P, et al. (2011) Atomic scale fluctuations govern brittle fracture and cavitation behavior in metallic glasses. *Phys Rev Lett* 107(21):215501.
- Wang YJ, Jiang MQ, Tian ZL, Dai LH (2016) Direct atomic-scale evidence for shear-dilatation correlation in metallic glasses. *Scr Mater* 112:37–41.
- Miracle DB (2004) A structural model for metallic glasses. *Nat Mater* 3(10):697–702.
- Sheng HW, et al. (2007) Polyamorphism in a metallic glass. *Nat Mater* 6(3):192–197.
- Chen DZ, et al. (2015) Fractal atomic-level percolation in metallic glasses. *Science* 349(6254):1306–1310.
- Ding J, Patinet S, Falk ML, Cheng Y, Ma E (2014) Soft spots and their structural signature in a metallic glass. *Proc Natl Acad Sci USA* 111(39):14052–14056.
- Ma E (2015) Tuning order in disorder. *Nat Mater* 14(6):547–552.
- Hafner J (1980) Theory of the formation of metallic glasses. *Phys Rev B* 21(2):406–426.
- Conner RD, Johnson WL, Paton NE, Nix WD (2003) Shear bands and cracking of metallic glass plates in bending. *J Appl Phys* 94:904–911.
- Zhu Z-D, Ma E, Xu J (2014) Elevating the fracture toughness of $\text{Cu}_{49}\text{Zr}_{42}\text{Hf}_9$ bulk metallic glass: Effects of cooling rate and frozen in excess volume. *Intermetallics* 46:164–172.
- Wang WH (2012) The elastic properties, elastic models and elastic perspectives of metallic glasses. *Prog Mater Sci* 57(3):487–656.
- An Q, et al. (2012) Predicted optimum composition for the glass-forming ability of bulk amorphous alloys: Application to Cu–Zr–Al. *J Phys Chem Lett* 3(21):3143–3148.
- Bernal JD (1960) Geometry of the structure of monatomic liquids. *Nature* 185:68–70.
- Cheng YQ, Sheng HW, Ma E (2008) Relationship between structure, dynamics, and mechanical properties in metallic glass-forming alloys. *Phys Rev B* 78:014207.
- Cheng YQ, Ma E (2011) Atomic-level structure and structure–property relationship in metallic glasses. *Prog Mater Sci* 56(4):379–473.
- Plimpton SJ (1995) Fast parallel algorithms for short-range molecular dynamics. *Comput Phys* 117(1):1–19.
- Ding J (2014) Local structure and structural signature underlying properties in metallic glasses and supercooled liquids. PhD thesis (Johns Hopkins University, Baltimore), pp 76–77.